

OPEN Oxygen conduction mechanism in Ca₃Fe₂Ge₃O₁₂ garnet-type oxide

Joohwi Lee , Nobuko Ohba & Ryoji Asahi

Received: 16 November 2018 Accepted: 17 January 2019 Published online: 22 February 2019

We investigate the oxygen conduction mechanism in a garnet-type oxide, Ca₃Fe₂Ge₃O₁₂, for the first time in detail by first-principle calculations. The nudged elastic band results confirm that this oxide has a lower migration barrier energy (0.45 eV) for an oxygen interstitial (O_i) with the kick-out mechanism than that (0.76 eV) for an oxygen vacancy. The migration paths for O_i are delocalized and connected to the neighboring cells in three-dimensional space. This oxide does not have a very low formation energy of O_i when the Fermi level is near the lowest unoccupied molecular orbital at a high temperature, which implies the possibility of electron doping by high-valence cations. These theoretical results suggest that the doping of Ca₃Fe₂Ge₃O₁₂ for generation of excess O_i provides a good oxygen-ion conductivity, along with the electronic conductivity.

Oxygen-ion conductors with high oxygen-ion conductivities (σ_0) have been developed owing to their desirable characteristics for applications as electrolytes of solid oxide fuel cells (SOFCs), oxygen separation membranes, and gas sensors^{1,2}. Nowadays, Y-doped (-stabilized) ZrO₂ (YSZ) is mostly used owing to its advantages such as abundance, chemical stability, nontoxicity, and low cost. It exhibits $\sigma_{\rm Q}$ of ~10⁻² S/cm at a high temperature (T) of \sim 1000 K (ref.³). In order to improve the industrial applicability, it is necessary to decrease its T while maintaining $\sigma_{\rm O}$. Some oxides such as Gd-doped CeO₂ (GDC)⁴, pure or Er-doped δ -phase of Bi₂O₃^{5,6}, and doped LaGaO₃⁷⁻¹¹, have higher σ_0 values at the same T than that of YSZ. However, a new type of oxygen-ion conductor with sufficient merits that can substitute YSZ is required.

Garnet-type oxides such as Li₇La₃Zr₂O

₁₂ (LLZO) have been reported as promising lithium-ion conductors¹²⁻¹⁶. This oxide has a high Li-ion conductivity when the cubic crystal structure is achieved in high temperature or stabilized by extrinsic dopants such as Nb and Ta. Partial occupancies of Li in unstable sites and formation of threedimensional channels are ascribed to high Li-ion conductivity^{14,15}. To the best of our knowledge, oxygen-ion conductions for the garnet-type oxides have not been widely investigated. Kubicek et al. 16, recently just reported that the oxygen-ion diffusivity in Ta-doped LLZO measured by isotope exchange experiment is comparable to the value in YSZ at 350 °C. Therefore, it is worth investigating an applicability of garnet-type oxides as oxygen-ion conductors.

It is necessary to know the properties relevant to σ_0 of a fundamental crystal structure, namely, normal garnet crystal structure with the composition of $A_3(^{2+})B_2(^{3+})C_3(^{4+})O_{12}$. We choose one of the stable garnet-type oxides, $Ca_3Fe_2Ge_3O_{12}$. This oxide could be grown as a single crystal by the flux method 17. First-principle databases such as Materials Project Database (MPD)¹⁸ suggest that this oxide forms the convex-hull state without separation into the mixture of other oxides. We investigated two important properties related to $\sigma_{\rm O}$, namely, formation energy (E_{form}) and migration barrier energy (E_{mig}) for both oxygen vacancy (V_O) and oxygen interstitial (O_i), in the Ca₃Fe₂Ge₃O₁₂ garnet-type oxide by first-principles calculations to clarify its oxygen-conduction mechanism.

Results and Discussion

Garnet crystal structure of Ca₃Fe₂Ge₃O₁₂. Figure 1 shows the garnet crystal structure of Ca₃Fe₂Ge₃O₁₂ belonging to the cubic crystal system with a space group of Ia-3d. Table 1 summarizes the internal coordinates, multiplicities, and Wyckoff positions of sites occupied by constituent chemical elements. The effective coordination numbers of Fe and Ge are natural numbers, 6 (in an octahedral site) and 4 (in a tetrahedral site), respectively, whereas that of Ca is ~7.8 [in a dodecahedral site (bisdisphenoid)]. The bond lengths of Fe–O and Ge–O significantly differ (2.05 and 1.79 Å, respectively). The Ca-O bond lengths, which are significantly longer than the above two lengths, slightly deviate; half of them are 2.41 Å, while the other half are 2.54 Å. All of the O atoms occupy the same sites, 96h, forming two, one, and one chemical bonds (in the tetrahedral site) with Ca, Fe, and Ge, respectively. Therefore, the $V_{\rm O}$ sites are identical to each other.

Toyota Central R&D Laboratories, Inc., Nagakute, Aichi, 480-1192, Japan. Correspondence and requests for materials should be addressed to J.L. (email: j-lee@mosk.tytlabs.co.jp)

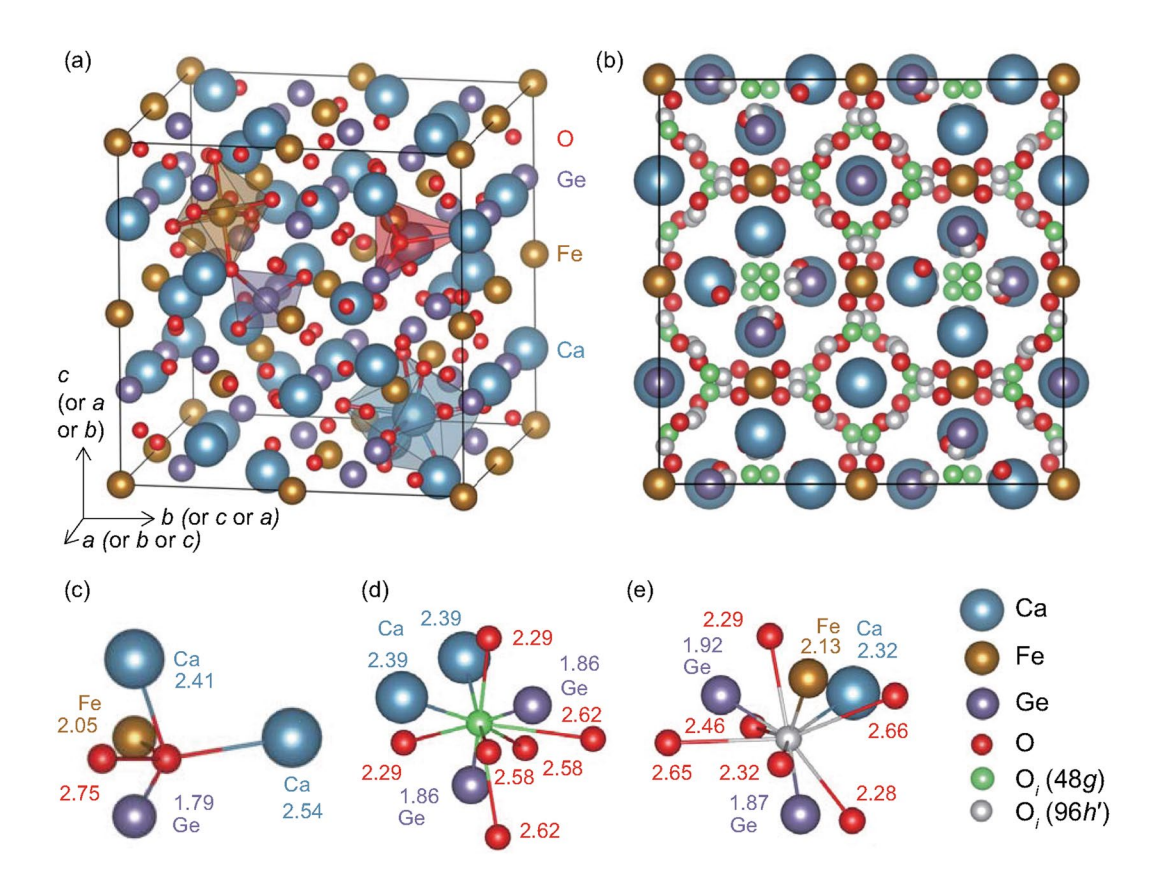


Figure 1. (a) Garnet crystal structure (space group: Ia-3d) of $Ca_3Fe_2Ge_3O_{12}$; the conventional cell with the cubic structure ($Ca_{24}Fe_{16}Ge_{24}O_{96}$, 160 atoms) is shown. (b) Distribution of equivalent 48g and 96h' sites after the optimization of the internal coordinates with one doubly charged O_i . The internal coordinates of the cations and O are equal to those of the perfect crystal; only the changes in the internal coordinates of O_i are shown in the optimized cells. In the calculations, one O_i is incorporated in the computational cell. Nearest-neighboring atoms of (c) O in the perfect crystal, (d) O_i in the 48g site, and (e) O_i in the 96h' site in the optimized structure including one O_i . The numerical values are the distances (bond lengths), expressed in \mathring{A} . The cutoff radius for the nearest-neighboring atoms in the figure is $2.8~\mathring{A}$, which is $\sim 10\%$ longer than the longest Ca-O bond.

Chemical element	Туре	Site multiplicity	Wyckoff letter	x	у	z
Ca (A ²⁺ cation)	Perfect crystal	24	с	1/4	1/8	0
Fe (B ³⁺ cation)	Perfect crystal	16	а	0	0	0
Ge (C4+ cation)	Perfect crystal	24	d	1/2	1/4	1/8
О	Perfect crystal	96	h	0.2834	0.0979	0.1989
O _i (16b)	Additional O _i	16	b	1/8	1/8	1/8
O _i (32e)	Additional O _i	32	е	0.1705	0.3295	0.6705
O _i (48g)	Additional O _i	48	g	0.8750 (0.8750) ^b	0.2704 (0.2734) ^b	0.4796 (0.4766) ^b
O _i (96h') ^a	Additional O _i	96	h	0.9167 (0.9074) ^b	0.3618 (0.3319) ^b	0.5368 (0.4856) ^b

Table 1. Internal coordinates of the constituent elements in the perfect crystal and initial internal coordinates of the O_i sites of the garnet-type $Ca_3Fe_2Ge_3O_{12}$ with the cubic crystal structure (160 atoms) before the optimization of the internal coordinates. The theoretical lattice parameter for this cubic crystal structure is 12.48 Å. ^aIn order to distinguish the Wyckoff letter of this O_i site from that of the O site in the perfect crystal, we denote this O_i site as 96h'. ^bThe internal coordinates of the O_i site with one O_i^{2-} after the relaxations are shown in the parentheses.

We consider several types of O_i sites. The initial positions of the O_i sites in the computations are summarized in Table 1, which were considered by an empty-space-finder module implemented in the MedeA program¹⁹. Among the four types of O_i sites, we focus on two sites, 48g and 96h', which are energetically stable and lead to satisfactory computational convergences. These O_i sites are shown in Figs 1 and Supplementary S1. The other two sites, 16h and 32h, are not analyzed in detail in this study, as we considered that they are not energetically preferred. When a neutral (O_i^0) and doubly charged oxygen interstitials (O_i^{2-}) occupy the 16h sites, the corresponding E_{form}

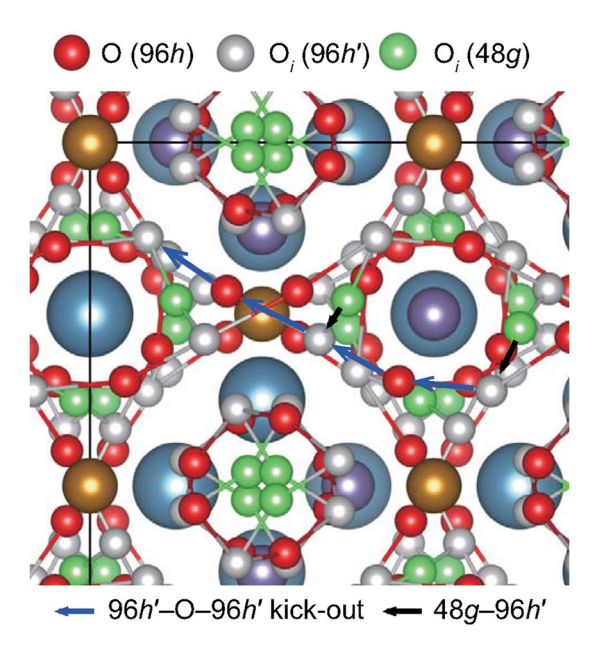


Figure 2. Two main migration paths of O_i and two types of equivalent O_i (48g and 96h') sites in the perfect crystal of the garnet-type $Ca_3Fe_2Ge_3O_{12}$. A part of the conventional cell of Fig. 1 is presented, showing all of the equivalent O_i sites. The colors representing the cations are the same as those in Fig. 1. The 96h'-O-96h' migration path with the kick-out mechanism is delocalized and connected to the neighboring cells in three-dimensional space.

values are 0.66 and 1.04 eV higher than those of the case where O_i occupy the most stable sites, respectively. The calculations with O_i in the 32e sites were not well converged, leading to a significantly higher energy and inability to satisfy the optimization condition.

 O_i in the 48g site participates in chemical bonds with two Ca and two Ge, whereas O_i in the 96h' site participates in chemical bonds with one Ca, one Fe, and two Ge. The bond lengths are optimized to be closer to their optimal values in the perfect crystal structure after relaxation of their internal coordinates. The Ca- O_i bond length is slightly shorter than the Ca-O bond length in the perfect crystal, whereas the Ge- O_i and Fe- O_i bond lengths are slightly longer than the Ge-O and Fe-O bond lengths in the perfect crystal, respectively. In addition, O_i in the 48g or 96h' sites participate in several bonds with O_i . The O_i - O_i bond lengths are generally longer than the cation- O_i bond lengths and shorter than the O_i - O_i distance in the perfect crystal structure, but some of them are similar to the Ca- O_i bond length.

 E_{mig} of an oxygen defect in $Ca_3Fe_2Ge_3O_{12}$. Regarding the oxygen-ion conduction, to the best of our knowledge, it is still not clear whether V_O or O_i is the dominant oxygen defect in the garnet-type oxides. In order to compare the migration barrier energies of V_O and O_i , we employ the climbing image nudged elastic band (CI-NEB) method^{20,21} for several candidates of migration paths. As the migrating oxygen defects, a doubly charged oxygen vacancy (V_O^{2+}) and O_i^{2-} are employed.

We show the investigated migration paths with E_{mig} among various migration paths in Supplementary Figs. S2 (for V_O^{2+}) and S3 (for O_i^{2-}). Two migration paths for O_i with low E_{mig} values among the various migration paths are considered in Fig. 2. One of them is the migration path between the 48g and 96h' sites with direct migration of O_i (48g–96h'), while the other is the migration path between two 96h' sites with the kick-out mechanism (96h'–O–96h'). Between the 48g and 96h' sites, the 48g site is more favorable to be occupied by O_i^{2-} . However, the distance between two 48g sites is as far as 3.16 Å, while the distance between 48g and 96h' sites is only 1.44 Å. This implies that direct migration of O_i can occur from the 48g site to the 96h' site with a low E_{mig} . Compared with the distance between the two 48g sites, the shortest distance between two 96h' sites is only 2.26 Å. In addition, another type of migration path based on the kick-out mechanism can exist. One O_i in the 96h' site moves to the O site; the kicked-out O atom moves to another O_i in the 96h' site. In this case, the distance between the 96h' site and O in the 96h site is only 1.9 Å. Combining the two migration paths, we suggest a long migration path between two 48g sites passing through the 96h' sites, as shown in Fig. 3(b). The 96h'–O–96h' migration path is delocalized and connected in the whole cell. If the 96h' site is more stable than the 48g site for O_i , the 48g–96h' migration path, which is localized, may not be needed to be considered for the lowest E_{mig} .

There is another migration path with a low E_{mig} (only 0.19 eV, 96h'—48g–96h' migration path) between two 96h' sites through the 48g site, as shown in Supplementary Fig. S3(c). However, as shown in Supplementary Fig. S4, this migration path is the same as the 48g–96h' migration path and is localized, so that the migration of O_i through the whole cell cannot occur only through this migration path. The 96h'–O–96h' migration path is additionally needed to connect through the whole cell, as mentioned above.

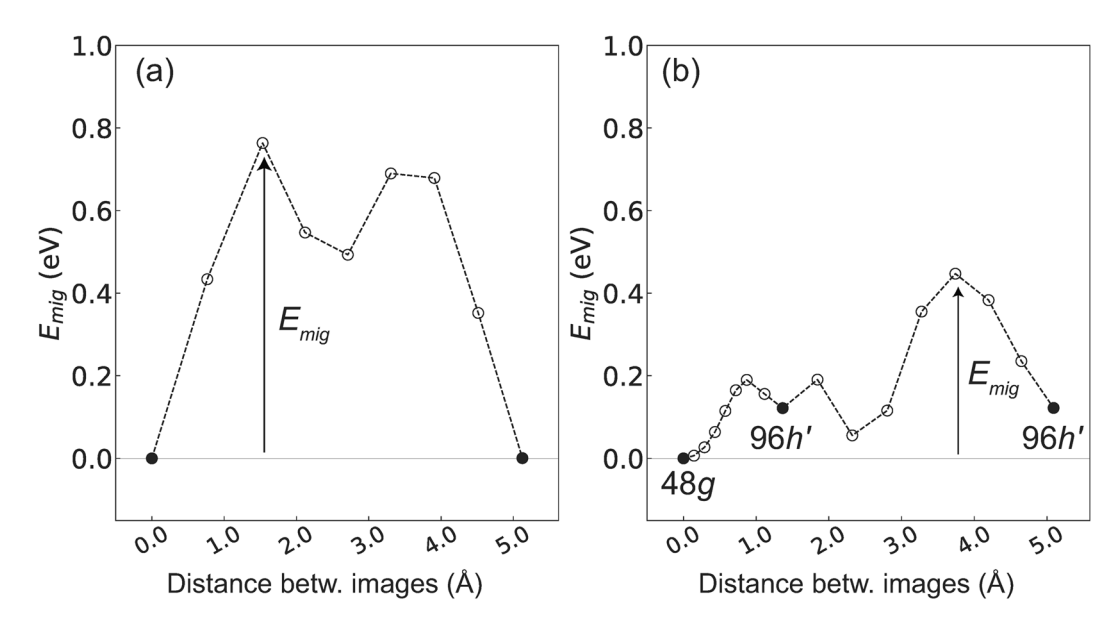


Figure 3. E_{mig} for (a) V_O and (b) O_i in the garnet-type $Ca_3Fe_2Ge_3O_{12}$. The oxygen defects are doubly charged. The closed circles denote the initial or final states, fixed in the CI-NEB method. Two migration paths for O_i , namely, the 48g-96h' direct migration and 96h'-O-96h' with the kick-out mechanism, are shown in Fig. 2.

Figure 3 shows the lowest E_{mig} obtained by the CI-NEB method among those of the considered migration paths for $V_{\rm O}$ and O_i . The intermediate procedures of movement of O_i along the 48g–96h' and 96h'–O–96h' migration paths are shown in Supplementary Figs S5 and S6. E_{mig} for O_i is significantly lower (0.45 eV) than that for $V_{\rm O}$ (0.76 eV). In addition, for the migration of $V_{\rm O}$ through the whole cell, E_{mig} higher than 0.76 eV with several combinations of migration paths is necessary because the migration path with E_{mig} of 0.76 eV is localized and not connected through the whole cell. This result suggests that the oxygen-ion conduction based on O_i with a significantly lower E_{mig} of 0.45 eV may be dominant. Therefore, the extrinsic doping with aliovalent cations with higher valences to make O_i rather than $V_{\rm O}$ can be useful to increase $\sigma_{\rm O}$ of $Ca_3Fe_2Ge_3O_{12}$.

 E_{form} of an oxygen defect in Ca₃Fe₂Ge₃O₁₂. It is worth investigating the formation condition of O_i utilizing its low E_{mig} . It is well known that E_{form} of an oxygen defect in an oxide compound strongly depends on the variables in equation (1) (see Method section.) such as the charge of the point defect (q), Fermi level (E_{Fermi}), and chemical potential of O_i (μ_O) depending on the pressure (p) and T_i (refs²²⁻²⁵). Figure 4(a) shows E_{form} of V_O and O_i as a function of E_{Fermi} at the O-rich condition (μ_O = half-energy of O_2). When E_{Fermi} is near the center of the band-gap [the band-gap of the garnet-type $Ca_3Fe_2Ge_3O_{12}$ obtained by the generalized gradient approximation (GGA) + U method is 2.15 eV], the neutral O_i^O is the most stable. When E_{Fermi} is shifted to a position near the highest occupied molecular orbital (HOMO, or valence band maximum), V_O^{2+} is stabilized (from the HOMO to 0.70 eV over the HOMO). When E_{Fermi} is shifted to the lowest unoccupied molecular orbital (LUMO, or conduction band minimum), O_i^{2-} is stabilized (from 1.77 eV over the HOMO to the LUMO). This result implies that O_i can be easily generated at the O-rich condition.

However, more realistic condition at a higher T should be considered for oxide synthesis and oxygen-ion conductor applications. Figure 4(b) shows E_{form} of $V_{\rm O}$ and O_i as a function of E_{Fermi} at p=1 atm and T=1000 K, which were selected based on the condition for the applications. $\mu_{\rm O}$ is obtained as the half-energy of O_2 minus 1.1 eV^{23,26}. When T increased to 1000 K, $V_{\rm O}^{2+}$ or $V_{\rm O}^{0}$ stabilized for most of the E_{Fermi} values. The E_{Fermi} range for stable O_i^{2-} at this T is only from 0.20 eV below the LUMO to the LUMO.

In order to reveal the thermodynamic stabilities of V_O and O_i in terms of p and T, we plot the difference in E_{form} between V_O and O_i [$\Delta E_{form}(O_i - V_O)$] at a fixed E_{Fermi} . Figure $\mathbf{4}(\mathbf{c})$ shows $\Delta E_{form}(O_i - V_O)$ when E_{Fermi} is at the center of the band-gap. When p is 1 atm, the T range for more stable O_i than V_O is below ~450 K. Figure $\mathbf{4}(\mathbf{d})$ shows $\Delta E_{form}(O_i - V_O)$ when E_{Fermi} is at the LUMO. Compared with the former condition, T for stable O_i increased to ~1100 K. However, it may not be sufficiently high because the usual sintering T for the oxides is higher than 1000 K. In addition, regardless of the location of E_{Fermi} the stabilizing T range for O_i generally decreases with the decrease in p. Therefore, in order to increase the O_i content, a high p for the oxygen-gas sources is required.

This result implies that O_i cannot be easily generated in $Ca_3Fe_2GeO_{12}$ despite its high potential for application as an oxygen-ion conductor. Processing at a lower T than ~1000 K may be necessary to provide O_i in $Ca_3Fe_2GeO_{12}$ by doping of aliovalent cations with higher valences than those of Ca, Fe, and Ge and thus increase E_{Fermi} to a level near the LUMO. However, the doped cations can also act as "electron donors". When positively charged defects such as La_{Ca}^+ are introduced by extrinsic doping, negative charges such as O_i^{2-} (for semiconductors, negatively charged defects are sometimes referred to as "electron killers?") and electrons are necessary to compensate for the charge imbalance. Therefore, a high E_{form} of O_i^{2-} implies the possibility of electron doping considering the charge neutrality requirement.

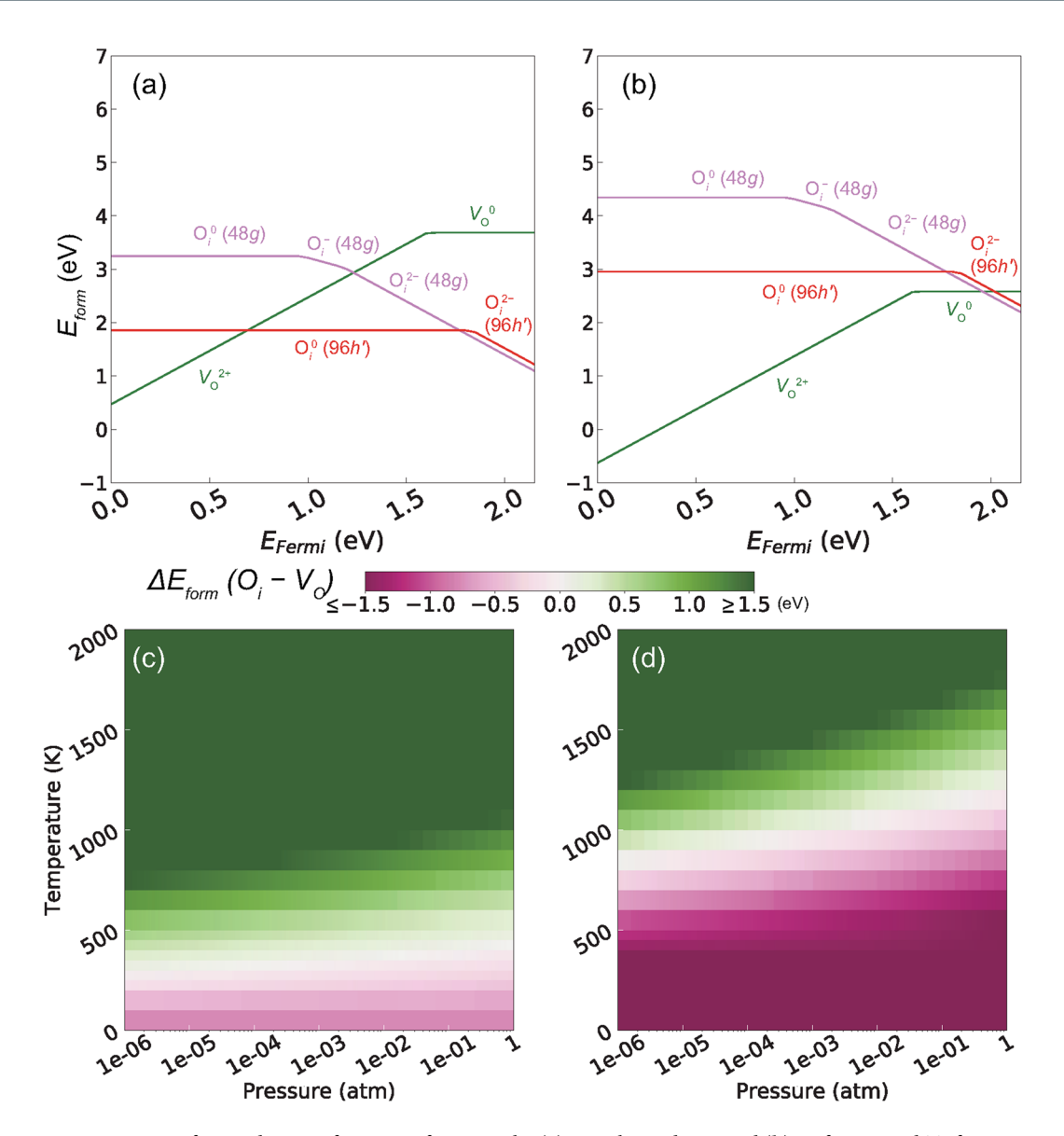


Figure 4. E_{form} of V_O and O_i as a function of E_{Fermi} at the (a) O-rich condition and (b) p of 1 atm and T of 1000 K for the garnet-type $Ca_3Fe_2Ge_3O_{12}$. $\Delta E_{form}(O_i-V_O)$ as a function of p and T when E_{Fermi} is (c) at the center of the band-gap and (d) at the LUMO. A negative $\Delta E_{form}(O_i-V_O)$ value implies that O_i preferentially forms compared to V_O .

In fact, our research group recently confirmed by a prediction model based on the machine learning technique and post-experiment that a La-doped $Ca_3Fe_2Ge_3O_{12}$ ($Ca_{2.7}La_{0.3}Fe_2Ge_3O_{12+\delta}$) with the garnet crystal structure has a good oxygen-ion conduction²⁸. However, its ionic transport number of σ_0 in the total conductivity ($\sim 10^{-2}$ S/cm at 700 °C) was $\sim 10\%$; therefore, the electronic conductivity was also observed. Considering theoretical results in this study and experimental results of ref.²⁸, we expect that both of excess O_i and electrons can be generated as transport carriers in $Ca_3Fe_2Ge_3O_{12}$ with doping of aliovalent cations with higher valences than those of Ca, Fe, and Ge.

As E_{form} of O_i^{2-} decreases with a gradient of -2, a lower E_{form} of O_i^{2-} near the LUMO can be achieved by increasing the band-gap. This suggests that band-gap engineering by mixing the constituent elements with others with the same valences can increase the band-gap, as in previous studies on $In_xGa_{1-x}N^{29}$, mixed anion lead halide perovskites³⁰, and Ni- and Co-doped ZnO nanoparticles³¹. In the $In_xGa_{1-x}N$ case, the LUMO increases as an increase of the Ga content because an energy level of Ga s is higher than that of In s, resulting in an increase of the band-gap. In the present case, Fe 3d forms the bottom of the LUMO, significantly below the unoccupied s levels of the other cations, as shown in Supplementary Fig. S7. Therefore, partial substitutions of trivalent cations, which can shift up the location of the LUMO from the Fe 3d levels, for Fe may be effective to increase the band-gap.

Finally, we calculated the formation energies of antisites (atomic interchange, a pair of X_Y and Y_X), which can be obtained by the differences in energies between supercells with and without antisites. The positions of the antisites were obtained by exchanging nearest-neighboring sites under the stoichiometric condition. The

generated antisites were not very stable. For most of the antisites, the energies increased by more than 1 eV, as shown in Supplementary Table 1. When Fe and O were exchanged, the structure became unstable, so that it was optimized to a perfect crystal without antisites. The high formation energies of cation antisites are reasonable because the local environments of the three types of cation sites are different in the garnet crystal structure³². The high formation energies of the cation antisites are also in agreement with the experimental result that $Ca_3Fe_2Ge_3O_{12}$ prefers to form the normal garnet crystal structure without inversion (exchange of cation sites)¹⁷. Moreover, the formation energies of oxygen antisites were larger than 5 eV, which indicates that oxygen cannot be easily incorporated in cation sites.

In summary, we investigated the oxygen-ion conduction mechanism in the $Ca_3Fe_2Ge_3O_{12}$ garnet-type oxide by the first-principles calculations. $Ca_3Fe_2Ge_3O_{12}$ exhibited a low E_{mig} of O_i of 0.45 eV with the kick-out mechanism. The migration path with this low E_{mig} was delocalized and connected to the neighboring cells in three-dimensional space. In addition, this value was lower than that of V_O of 0.76 eV. However, this oxide had a shallow range of E_{Fermi} just below the LUMO to form O_i at a practical T of 1000 K. This implies that high concentrations of extrinsic dopants, which may act as electron donors, are needed. Therefore, we expect that processing at a low T and band-gap engineering to achieve a larger band-gap and thus generate stable O_i are needed to achieve and improve σ_O of this oxide.

The findings in this study provide valuable insights, which can inspire further investigations on the garnet-type oxygen-ion conductors. The proposed computational strategy can be employed for analyses of other combinations with this crystal structure.

Method

All of the first-principles calculations were performed using the projector augmented wave (PAW)^{33,34} method implemented in the Vienna *Ab-initio* Simulation Package (VASP)^{35,36}. We used the GGA exchange–correlation functional parameterized in the Perdew–Burke–Ernzerhof (PBE) form³⁷ along with the on-site Coulomb interaction³⁸ with an effective U-J of 4.3 eV (GGA + U) for the d-orbitals of Fe. This was implemented because the band-gap obtained by the GGA method was only 0.1 eV. Owing to the lack of references for Ca₃Fe₂Ge₃O₁₂, the value of U-J was selected using previous theoretical calculations for α -Fe₂O₃^{24,39}, which has the same valence of Fe³⁺. Mosey *et al.*³⁹ proposed a reasonable U-J value, which converged well with the increase in the computational unit of α -Fe₂O₃, and confirmed that GGA+U with U-J of 4.3 eV was in good agreement with the lattice parameter, volume, bulk modulus, and band-gap obtained in experiments. We confirmed that the lattice parameter (12.48 Å) of Ca₃Fe₂Ge₃O₁₂ obtained by GGA+U is in good agreement with the corresponding value (12.32 Å) obtained in the experiment¹⁷.

The structural relaxations of the primitive cells (80 atoms) with the associated changes in lattice constants and atomic coordinates were performed until the interatomic force on each atom was reduced below $0.005\,\text{eV}$ /Å. The cutoff energy was set to 500 eV. The Brillouin zone was sampled using Γ -centered $4\times4\times4$ meshes. Brillouin zone integrations were performed using Gaussian smearing with a smearing width of $0.1\,\text{eV}$. Electron spin polarizations were turned on.

We also computed E_{form} and E_{mig} as their low values are favorable for a higher $\sigma_0^{40,41}$. The E_{form} values were computed using the conventional cubic cell (160 atoms with a lattice constant larger than 10 Å)²²:

$$E_{form}^{q} = E(\text{Ca}_{3}\text{Fe}_{2}\text{Ge}_{3}\text{O}_{12}: D^{q}) - E(\text{Ca}_{3}\text{Fe}_{2}\text{Ge}_{3}\text{O}_{12}) - n_{D}\mu_{O} + q(E_{\text{HOMO}} + E_{Fermi}) + \Delta E_{LZ}, \tag{1}$$

where $E(\text{Ca}_3\text{Fe}_2\text{Ge}_3\text{O}_{12}:D^q)$ is the energy of a supercell including a point defect $(V_0 \text{ or } O_i)$, $E(\text{Ca}_3\text{Fe}_2\text{Ge}_3\text{O}_{12})$ is the energy of a supercell of the perfect $\text{Ca}_3\text{Fe}_2\text{Ge}_3\text{O}_{12}$, n_D is 1 (or -1), which corresponds to the interstitial defect (or vacancy), μ_0 is the chemical potential of an added (or removed) O, q is the charge of the point defect, E_{HOMO} is the eigenvalue of the HOMO formed mainly by O 2p, E_{Fermi} is the Fermi level as a variable, and ΔE_{1Z} is the correction term proposed by Lany and Zunger^{42,43} to compensate the image charge interactions between supercells for the charged point defect. The calculations using the supercell including a defect were performed until the interatomic forces on each atom were reduced below $0.02\,\text{eV}/\text{Å}$ at a fixed lattice constant. Only the Γ -point was used for the k-space sampling. The computed energy differences between the primitive and conventional cells were below $\sim 1\,\text{meV}/\text{atom}$. The transformations between the primitive and conventional cells were performed by SPGLIB⁴⁴ implemented in PHONOPY^{45,46}. The dielectric constant (13.0 for $\text{Ca}_3\text{Fe}_2\text{Ge}_3\text{O}_{12}$) for the correction term of the image charge interaction 42,43 was computed using the primitive cell based on the density functional perturbation theory⁴⁷. The supercells with point defects were created by removing or adding twice more electrons compared to the number of removed or added oxygen atoms to compensate the background charges. For the neutral O_i , the nonmagnetic state (compensated spin polarization) was used as its energy was significantly lower (more than 1 eV) than that of the ferromagnetic state (magnetic moment of 2).

The E_{mig} values were calculated using the CI-NEB method 20,21 with three intermediate images. When the convergence of the computation was not satisfactory or when more detailed migration paths should be investigated, seven intermediate images were employed. The CI-NEB calculations were performed until the forces decreased below $0.03\,\mathrm{eV/Å}$ with a spring constant of $5\,\mathrm{eV/Å}^2$ between the images. We employed a doubly charged oxygen vacancy (V_O^{2+}) and oxygen interstitial $(\mathrm{O_i}^{2-})$ for E_{mig} assuming that these charged point defects were formed by extrinsic doping with aliovalent cations. Visualizations of the crystal structures and confirmation of the effective coordination numbers of the cations were performed using the VESTA program 48 .

References

- 1. Knauth, P. & Tuller, H. L. Solid-state ionics: roots, status, and future prospects. J. Am. Ceram. Soc. 85, 1654-1680 (2002).
- 2. Skinner, S. J. & Kilner, J. A. Oxygen ion conductors. Mater. Today 6, 30-37 (2003).
- 3. Gellings, P. J. & Bouwmeester, H. Handbook of solid state electrochemistry (CRC press, 1997).

- Mogensen, M., Sammes, N. M. & Tompsett, G. A. Physical, chemical and electrochemical properties of pure and doped ceria. Solid State Ion. 129, 63–94 (2000).
- 5. Sammes, N., Tompsett, G., Näfe, H. & Aldinger, F. Bismuth based oxide electrolytes—structure and ionic conductivity. *J. Eur. Ceram. Soc.* 19, 1801–1826 (1999).
- Shitara, K. et al. First-principles selection of solute elements for Er-stabilized Bi₂O₃ oxide-ion conductor with improved long-term stability at moderate temperatures. Chem. Mater. 29, 3763–3768 (2017).
- Ishihara, T., Matsuda, H. & Takita, Y. Doped LaGaO₃ perovskite type oxide as a new oxide ionic conductor. J. Am. Chem. Soc. 116, 3801–3803 (1994).
- 8. Drennan, J. et al. Characterisation, conductivity and mechanical properties of the oxygen-ion conductor La_{0.9}Sr_{0.1}Ga_{0.8}Mg_{0.2}O_{3-x}. J. Mater. Chem. 7, 79–83 (1997).
- 9. Huang, K. & Goodenough, J. B. A solid oxide fuel cell based on Sr- and Mg-doped LaGaO₃ electrolyte: the role of a rare-earth oxide buffer. *J. Alloys Compd.* **303**, 454–464 (2000).
- Ishihara, T., Shibayama, T., Honda, M., Nishiguchi, H. & Takita, Y. Intermediate temperature solid oxide fuel cells using LaGaO₃ electrolyte II. Improvement of oxide ion conductivity and power density by doping Fe for Ga site of LaGaO₃. J. Electrochem. Soc. 147, 1332–1337 (2000).
- 11. Gao, Z., Miller, E. C. & Barnett, S. A. A high power density intermediate-temperature solid oxide fuel cell with thin $(La_{0.9}Sr_{0.1})_{0.98}(Ga_{0.8}Mg_{0.2})O_{3-\delta}$ electrolyte and nano-scale anode. *Adv. Func. Mater.* **24**, 5703–5709 (2014).
- Kokal, I., Somer, M., Notten, P. & Hintzen, H. Sol-gel synthesis and lithium ion conductivity of Li₇La₃Zr₂O₁₂ with garnet-related type structure. Solid State Ion. 185, 42–46 (2011).
- 13. Meier, K., Laino, T. & Curioni, A. Solid-state electrolytes: revealing the mechanisms of Li-ion conduction in tetragonal and cubic LLZO by first-principles calculations. *J. Phys. Chem. C* 118, 6668–6679 (2014).
- Jalem, R. et al. Concerted migration mechanism in the Li ion dynamics of garnet-type Li₇La₃Zr₂O₁₂. Chem. Mater. 25, 425–430 (2013).
- 15. Miwa, K. & Asahi, R. Molecular dynamics simulations with machine learning potential for Nb-doped lithium garnet-type oxide $\text{Li}_{7-x}\text{La}_3(\text{Zr}_{2-x}\text{Nb}_x)\text{O}_{12}$. Phys. Rev. Mater. 2, 105404 (2018).
- 16. Kubicek, M. et al. Oxygen vacancies in fast lithium-ion conducting garnets. Chem. Mater. 29, 7189-7196 (2017).
- 17. Lévy, D. & Barbier, J. Normal and inverse garnets: Ca₃Fe₂Ge₃O₁₂, Ca₃Y₂Ge₃O₁₂ and Mg₃Y₂Ge₃O₁₂. Acta Crystallogr. C 55, 1611–1614 (1999).
- 18. Jain, A. et al. Commentary: The Materials Project: A materials genome approach to accelerating materials innovation. Appl. Phys. Lett. Mater. 1, 011002 (2013).
- 19. Materials Design, Inc. MedeA. https://www.materialsdesign.com/medea (2018).
- 20. Henkelman, G., Uberuaga, B. P. & Jónsson, H. A climbing image nudged elastic band method for finding saddle points and minimum energy paths. *J. Chem. Phys.* 113, 9901–9904 (2000).
- 21. Henkelman, G. & Jónsson, H. Improved tangent estimate in the nudged elastic band method for finding minimum energy paths and saddle points. *J. Chem. Phys.* 113, 9978–9985 (2000).
- 22. Van de Walle, C. G. & Neugebauer, J. First-principles calculations for defects and impurities: Applications to III-nitrides. J. Appl. Phys. 95, 3851–3879 (2004).
- 23. Reuter, K. & Scheffler, M. Composition, structure, and stability of RuO₂ (110) as a function of oxygen pressure. *Phys. Rev. B* **65**, 035406 (2001).
- 24. Lee, J. & Han, S. Thermodynamics of native point defects in α-Fe₂O₃: an *ab initio* study. *Phys. Chem. Chem. Phys.* **15**, 18906–18914 (2013).
- 25. Oba, F., Togo, A., Tanaka, I., Paier, J. & Kresse, G. Defect energetics in ZnO: A hybrid Hartree-Fock density functional study. *Phys. Rev. B* 77, 245202 (2008).
- 26. Stull, D. R. & Prophet, H. JANAF thermochemical tables (1971).
- 27. Zunger, A. Practical doping principles. *Appl. Phys. Lett.* **83**, 57–59 (2003).
- 28. Kajita, S., Ohba, N., Suzumura, A., Tajima, S. & Asahi, R. Discovery of superionic conductors by ensemble-scope descriptor. Submitted. (2018).
- 29. Davydov, V. Y. et al. Band gap of InN and In-rich $In_xGa_{1-x}N$ alloys (0.36 < x < 1). Phys. Status Solidi B 230, R4–R6 (2002).
- 30. Kulkarni, S. A. et al. Band-gap tuning of lead halide perovskites using a sequential deposition process. J. Mater. Chem. A 2, 9221–9225 (2014).
- 31. Ali, R. N. et al. Band gap engineering of transition metal (Ni/Co) codoped in zinc oxide (ZnO) nanoparticles. J. Alloys Compd. 744, 90–95 (2018).
- 32. Ye, W., Chen, C., Wang, Z., Chu, I.-H. & Ong, S. P. Deep neural networks for accurate predictions of crystal stability. *Nat. Comm.* 9, 3800 (2018).
- 33. Blöchl, P. E. Projector augmented-wave method. Phys. Rev. B 50, 17953-17979 (1994).
- 34. Kresse, G. & Joubert, D. From ultrasoft pseudopotentials to the projector augmented-wave method. *Phys. Rev. B* **59**, 1758–1775 (1999).
- 35. Kresse, G. & Furthmüller, J. Efficiency of ab-initio total energy calculations for metals and semiconductors using a plane-wave basis set. *Comput. Mater. Sci.* **6**, 15–50 (1996).
- 36. Kresse, G. & Furthmüller, J. Efficient iterative schemes for *ab initio* total-energy calculations using a plane-wave basis set. *Phys. Rev. B* **54**, 11169–11186 (1996).
- 37. Perdew, J. P., Burke, K. & Ernzerhof, M. Generalized gradient approximation made simple. Phys. Rev. Lett. 77, 3865-3868 (1996).
- 38. Dudarev, S. L., Botton, G. A., Savrasov, S. Y., Humphreys, C. J. & Sutton, A. P. Electron-energy-loss spectra and the structural stability of nickel oxide: An LSDA + U study. *Phys. Rev. B* 57, 1505–1509 (1998).
- 39. Mosey, N. J., Liao, P. & Carter, E. A. Rotationally invariant *ab initio* evaluation of Coulomb and exchange parameters for DFT + U calculations. *J. Chem. Phys.* **129**, 014103 (2008).
- 40. Singhal, S. C. & Kendall, K. High-temperature solid oxide fuel cells: fundamentals, design and applications (Elsevier, 2003).
- 41. Lee, J., Ohba, N. & Asahi, R. Discovery of zirconium dioxides for the design of better oxygen-ion conductors using efficient algorithms beyond data mining. RSC Adv. 8, 25534–25545 (2018).
- 42. Lany, S. & Zunger, A. Assessment of correction methods for the band-gap problem and for finite-size effects in supercell defect calculations: Case studies for ZnO and GaAs. *Phys. Rev. B* 78, 235104 (2008).
- Lany, S. & Zunger, A. Accurate prediction of defect properties in density functional supercell calculations. Modell. Simul. Mater. Sci. Eng. 17, 084002 (2009).
- 44. Togo, A. & Tanaka, I. Spglib: a software library for crystal symmetry search. arXiv 1808.01590, 1-11 (2018).
- 45. Togo, A., Oba, F. & Tanaka, I. First-principles calculations of the ferroelastic transition between rutile-type and CaCl₂-type SiO₂ at high pressures. *Phys. Rev. B* 78, 134106 (2008).
- 46. Togo, A., Chaput, L., Tanaka, I. & Hug, G. First-principles phonon calculations of thermal expansion in Ti₃SiC₂, Ti₃AlC₂, and Ti₃GeC₂. *Phys. Rev. B* **81**, 174301 (2010).
- 47. Baroni, S., Giannozzi, P. & Testa, A. Green's-function approach to linear response in solids. Phys. Rev. Lett. 58, 1861–1864 (1987).
- Momma, K. & Izumi, F. VESTA 3 for three-dimensional visualization of crystal, volumetric and morphology data. J. Appl. Crystallogr. 44, 1272–1276 (2011).

Acknowledgements

The authors thank Drs. Shin Tajima, Seiji Kajita, and Hiroshi Ohno in Toyota Central R&D Lab. for fruitful discussions.

Author Contributions

J.L. proposed the idea for computational works and carried out the first principles calculations. N.O. and R.A. advised the strategy of the research. All authors analyzed theoretical data, discussed the results, and wrote the manuscript.

Additional Information

Supplementary information accompanies this paper at https://doi.org/10.1038/s41598-019-39288-x.

Competing Interests: The authors declare no competing interests.

Publisher's note: Springer Nature remains neutral with regard to jurisdictional claims in published maps and institutional affiliations.

Open Access This article is licensed under a Creative Commons Attribution 4.0 International License, which permits use, sharing, adaptation, distribution and reproduction in any medium or format, as long as you give appropriate credit to the original author(s) and the source, provide a link to the Creative Commons license, and indicate if changes were made. The images or other third party material in this article are included in the article's Creative Commons license, unless indicated otherwise in a credit line to the material. If material is not included in the article's Creative Commons license and your intended use is not permitted by statutory regulation or exceeds the permitted use, you will need to obtain permission directly from the copyright holder. To view a copy of this license, visit https://creativecommons.org/licenses/by/4.0/.

© The Author(s) 2019